Title: Polymer Microarray with Tailored Morphologies through Condensed Droplet Polymerization for High-Resolution Optical Imaging Applications

*Kwang-Won Park[1], Sophie S. Liu[1,2], Wenjing Tang[1], and Rong Yang[1,2]**

K. Park, S. S. Liu, W. Tang, R. Yang
Robert F. Smith School of Chemical and Biomolecular Engineering
Cornell University, Ithaca, NY 14853
United States
E-mail: ryang@cornell.edu

S. S. Liu, R. Yang
Meinig School of Biomedical Engineering
Cornell University, Ithaca, NY 14853
United States

Keywords: condensed droplet polymerization, polymer dome arrays, wetting properties, tunable morphology of surface structure, nanoscale optical lenses

Abstract: Nature-inspired functional surfaces with micro- and nanoscale features have garnered interest for potential applications in optics, imaging, and sensing. Traditional fabrication methods, such as lithography and self-assembly, face limitations in versatility, scalability, and morphology control. This study introduces an innovative technology, condensed droplet polymerization (CDP), for fabricating polymeric micro- and nano-dome arrays (PDAs) with readily tunable geometric properties—a challenging feat for conventional methods. The CDP process leverages free-radical polymerization in condensed monomer droplets, allowing rapid production of PDAs with targeted sizes, radii of curvature, and surface densities by manipulating a key synthesis parameter: the temperature of a filament array that activates initiators. We systematically unravel its effects on polymerization kinetics, viscoelastic properties of the polymerizing droplets, and geometric characteristics of the PDAs. Utilizing in-situ digital microscopy, we reveal the morphological evolution of the PDAs during the process. The resulting PDAs exhibit distinct optical properties, including magnification that enables high-resolution imaging beyond the diffraction limit of

conventional microscopes. We demonstrate the ability to magnify and focus light, enhancing imaging of subwavelength structures and biological specimens. This work advances our understanding of polymerization mechanisms in nano-sized reactors (i.e., droplets) and paves the way for developing compact optical imaging and sensing technologies.

1. Introduction

Nature thrives and evolves by employing effective designs of structured functional surfaces to address complex challenges. For example, the multifunctional biomineralized armor of the chiton *Acanthopleura granulate* comprises hundreds of aragonite-based microscopic lenses, allowing the chiton to detect light and potentially resolve images.[1] Insects and birds (e.g., *Ophiocoma wendtii, Morpho rhetenor* butterflies, and *Tachycineta bicolor* birds) exhibit unique optical properties and structural colors that enhance their photosensitivity while camouflaging themselves, which originate from micro- or nanoscale photonic structures.[2] Over the past two decades, inspired by these properties afforded by nature, micro- or nano-lenses have been of particular interest for the application of compact optical systems for sensing, imaging, and microlithogrphy.[3]

Among the material candidates, polymers have emerged as one of the most influential ones for fabricating structured functional surfaces due to their suitable mechanical properties, processability, and low cost. Additionally, polymers afford a rich palette of functional groups that enables tunable refractive index and points to simultaneous sensing, imaging, and actuation.[4] Current methodologies for fabricating micro- and nano-structured polymeric surfaces predominantly rely on two approaches. The top-down processes, such as lithography, etching, or machining, deliver limited flexibility in the lens geometry.[5] Moreover, these methods are hard to scale as the process of generating curvature in the z-direction tends to be laborious and affords limited tunability in the size and shape of the individual lenses.[5a, 5b] Consequently, bottom-up approaches, including self-assembly or 3D printing, have been suggested as alternatives.[6] Kim et al. have demonstrated the creation of dome-shaped particles, namely nanolenses, by the crystallization of organic molecules for near-field focusing and magnification.[7] However, the fabrication of lens array is challenging due to low yield and poor control over the solution crystallization process. Recently, inkjet and 3D printing approaches have been widely used to directly print microlens arrays on solid surfaces.[3c, 6a] The printing methods could control surface geometries, such as size ranging from micro- to meso-scale as well as profiles determined by the contact angle of the monomer

droplets on the surface. However, they deliver limited scalability over large areas, as well as precision in surface geometry, especially the radius of curvature. In general, lens arrays require days, if not weeks, to fabricate, critically limiting their manufacturing and deployment.

Here, we tackle those significant challenges in nanomaterial synthesis by employing an innovative technique known as condensed droplet polymerization (CDP). This emerging technology facilitates free-radical polymerization within monomer microdroplets that are condensed from vapor-phase reactants, representing a paradigm shift in the field.[8] We present compelling evidence that CDP enables the rapid production of soft microdome arrays at the wafer scale in mere minutes, marking a substantial advancement in the synthesis and manufacturing processes of nanomaterials. Notably, a key innovation of our approach lies in the programmability of the geometric properties of the arrays—including dome size, radius of curvature, and surface density—achieved through straightforward adjustments of a critical synthesis parameter, specifically the temperature of the filament used to activate the initiator. This level of control is unprecedented in existing synthesis and fabrication methods, demonstrating a marked improvement in the ability to tailor material properties to specific applications. Our findings are grounded in a novel theoretical framework that elucidates the triadic relationship among reaction kinetics, the rheological properties of a polymerizing droplets, and non-equilibrium phase transitions. This framework not only supports our experimental observations but also offers a deeper understanding of the underlying mechanisms at play. We demonstrate the potential impacts of this tailored control in the fields of optics, where we utilize the polymer dome arrays as plano spherical convex lenses for the optical imaging of nanoscale and microscale objects. By exploiting their tunable focal lengths, we have designed and synthesized polymer lenses capable of resolving features that surpass the diffraction limit of conventional optical microscopes. This groundbreaking capability unlocks a plethora of avenues for high-resolution optical imaging and sensing applications, thereby expanding the frontiers of what is achievable in nanotechnology.

2. Results and Discussion

2.1. The in-situ and real-time observation of the condensed droplet polymerization (CDP) process.

The CDP process was used to polymerize monomer (micro)droplets to obtain polymer micro- or nano-dome arrays (PDAs) (**Figure 1**a,b). The process begins with placing a

poly(1H,1H,2H,2H-perfluorodecyl acrylate) (pPFDA)-coated Si wafer on a thermoelectric cooling (TEC) device inside a cylindrical vacuum chamber. Benzyl methacrylate (BzMA) monomer is vaporized and introduced into the chamber to condense, in a dropwise fashion, on the cooled pPFDA surface. Subsequently, *tert*-butyl peroxide (TBPO) is introduced and thermally decomposed to generate reactive radicals upon passing a filament heater placed inside the vacuum chamber. The radicals diffuse into the monomer droplets and initiate the free radical polymerization of BzMA (Figure 1c). As a last step, the chamber was evacuated to remove unreacted precursors from the droplets and yield solid PDAs. The successful obtainment of quasi-hexagonal arrays of pBzMA PDAs via CDP was confirmed using scanning electron microscopy (SEM), as shown in Figure 1d.

The in-situ monitoring of the time-evolution of droplet size and morphology throughout the CDP process is enabled by a long-focal-length digital microscope, with the representative top-down images that correspond to each phase of CDP highlighted in Figure 1a, namely (i) monomer dropwise condensation, (ii) droplet polymerization, and (iii) chamber evacuation. Within each phase, the detailed time course of the droplet evolution is shown in **Figures 2**a-c. During phase I, BzMA vapor undergoes dropwise condensation as its partial pressure (P_M) exceeds the saturation pressure ($P_{M,sat}$) at the substrate temperature (T_{sub}), i.e., 10 °C. Unlike other CDP polymerization process, where precursors are commonly maintained under sub-saturation conditions ($P_M/P_{M,sat} < 1$),[9] CDP deliberately leverages supersaturated conditions ($P_M/P_{M,sat} >> 1$) to enable condensation and micro-/nanodroplet formation.[8] Accordingly, we estimate a $P_M/P_{M,sat}$ of 5.0 for the conditions employed (i.e., P_{BzMA} = 50 mTorr, T_{sub} = 10 °C), which ensures rapid dropwise condensation. Condensation was allowed to continue until the desired droplet size was reached, e.g., a duration of 60 s leads to vast arrays of BzMA monomer droplets with diameters of 30 - 40 μm (Figure 2a).

Phase II involves rapid polymerization of the monomer droplets (Figure 2b). To minimize further adsorption or condensation of monomer vapors during this stage, we ceased the monomer influx; only TBPO vapor was continuously delivered until the desired pressure was reached (100 ~ 300 mTorr). A filament heater thermally dissociates the initiator TBPO to form *tert*-butoxy (*t*-BuO•) and/or methyl (CH_3•) radicals (Figure 1c). The dominating radical species can be controlled by manipulating the filament temperature (T_{fil}) in the range of 220 to 340 °C, with lower T_{fil} favoring *t*-BuO• and higher T_{fil} favoring CH_3•.[9] Upon contacting the droplets, these radicals initiate chain-growth polymerization. The process resembles mini-

emulsion polymerization due to the phase boundary, albeit a vapor-liquid boundary instead of a liquid-liquid one, and the small size of the polymerizing droplets.[10] Chain propagation in sustained by the rapid diffusion of unreacted BzMA monomer to the surface of polymerizing droplets.[8b] Additionally, the low T_{sub} (10 °C) inhibits monomer evaporation, stabilizing the size of the polymerizing droplets throughout phase II.

In phase III, polymerization reactions are terminated by stopping the TBPO flow and bringing the chamber down to base pressure (10 mTorr). Within a minute, the unreacted precursors are removed from the partially polymerized droplets, yielding solid PDAs (Figure 2c). To ensure complete removal of unreacted precursors, the base pressure is maintained for an additional 5 min after phase III.

A comparison of the size distributions by the end of phase I, representing condensed (unreacted) monomer droplets, and those by the end of phase III, representing PDAs, reveals a significant decrease in size (Figure S1, Supporting Information). The unreacted monomer droplets exhibit a broad diameter distribution, i.e., 24.6 ± 10.5 μm, whereas the resulting PDAs show a narrower distribution, i.e., 12.0 ± 2.4 μm. Furthermore, superimposing the optical micrographs obtained at the beginning and the end of phase III (Figure S1b, Supporting Information) illustrates that the partially polymerized droplets contract isotropically toward the center during phase III. This results in PDAs with isotropic dome shapes, as confirmed by the surface height scans obtained using 3D atomic force microscopy (AFM, Figure 2d). The AFM line profile further validates the smooth surface and the nearly spherical cap shape of the PDAs. Additionally, 2D AFM images demonstrate the smooth surface of the pPFDA base layer, with a root mean square roughness (R_{rms}) of 5.3 nm (Figure S2, Supporting Information). It is important to note that due to the significant height difference between the PDA and the surface, the pPFDA base layer is nearly invisible within the color range of 0 to 600 nm, while the contour of PDA is observed properly. No further dome contraction was observed after the initial 45 s of phase III, suggesting that the final PDAs contain negligible precursors. This was confirmed using FT-IR, where the C=C stretching peak at 1640 cm^{-1} (from unreacted monomers) was absent from the spectrum of the resulting PDAs (Figure S3, supporting information).

Within each droplet, the monomer consumption rate, i.e., monomer conversion (%), was determined by dividing the estimated volumes of the PDAs by those of the unreacted droplets

(via superimposing the micrographs from the same CDP run, Figure 2e). It is linearly proportional to the polymerization time, i.e., the duration of phase II. As such, larger PDAs can be obtained simply by prolonging the polymerization time. Interestingly, CDP produces tens-of-micron-sized PDAs within a few minutes, which, combined with its scalability,[11] makes CDP a promising technology for the manufacturing of PDAs over large areas. By comparison, emulsion polymerization under UV irradiation, while relatively rapid among existing polymerization techniques, requires 30 min to produce polymer particles of smaller sizes (~1 μm in diameter).[12]

2.2. Polymer morphologies controlled via filament temperature (T_{fil})

To clearly explain the effects of T_{fil} on the PDA morphology, below, we focus on describing our experimental observations. A detailed mechanistic discussion is provided in section **2.3 Mechanisms of tailoring PDA morphologies**.

2.2.1. T_{fil} affects the average diameter of PDAs

Building upon the uniform size distribution of the PDAs obtained under a specific set of synthesis conditions (as detalied in Table S1, Supporting Information), we further hypothesize that the average PDA diameter can be controlled by tuning the synthesis conditions. Below, we illustrate that tunability by varying T_{fil} and focus on its impact on the polymerization kinetics, which in trun led to larger PDAs at higher T_{fil} (**Figure 3**a-c).

We performed CDP at T_{fil} of 220, 280, and 340 °C, respectively, with P_{BzMA} = 300 mTorr, $t_{polymerization}$ = 2 min, T_{sub} = 10 °C. The diameter distributions of the condensed monomer droplets before polymerization (phase I, see Figures 3d-f, blue) were quantified based on the micrographs collected in-process. A similar average diameter of ~50 μm was observed for all T_{fil}, confirming that the polymerization (phase II) had comparable starting points. The diameters of the PDAs obtained at the end of CDP were 21.1 ± 3.9, 23.0 ± 3.8, and 31.2 ± 6.7 μm at the T_{fil} of 220, 280, and 340 °C, respectively, as measured from micrographs (Figure 3d-f, red). Furthermore, this trend persists regardless of the initiator concentration (Figure S4, Supporting Information). As the initiator partial pressure P_{TBPO} was varied from 100 to 300 mTorr, higher T_{fil} values consistently gave rise to larger average diameters of PDAs.

2.2.2. T_{fil} affects the radius of curvature of PDAs

To fully characterize the morphological properties of the PDAs, we quantified the height and diameter of each polymer dome using cross-sectional SEM images (Figure 3g,h). The 3D morphology was described using the radius of curvature and aspect ratio (i.e., the height-to-diameter ratio), which vary considerably with the T_{fil} used during CDP. The PDAs prepared at a T_{fil} of 220 °C exhibited a radius of curvature of 12.0 ± 3.4 μm corresponding to an aspect ratio of 0.28 ± 0.03 (Figure 3i). These dimensions point to a more spherical dome shape compared to those prepared at T_{fil} of 280 °C or 340 °C, showing radii of curvature of 14.2 ± 2.4 and 22.5 ± 4.9 μm, corresponding aspect ratios of 0.23 ± 0.02 and 0.21 ± 0.03, respectively. The radii of curvature were calculated by assuming a spherical cap shape, which is valid due to the droplet's small size and, hence, the negligible effect of gravity, which was confirmed by AFM (Figure 2d). Notably, the ability to manipulate the radius curvature of PDAs is crucial for the functionality and performance of plano-spherical convex lenses in various applications, as detailed in Section **2.4 Nanolens Applications.**

2.2.3. T_{fil} affects the surface density of PDAs in conjunction with the condensation time.
Additionally, we observed that the surface density of PDAs could be manipulated by simultaneously manipulating the condensation time (phase I) and T_{fil} (phase II), as shown in **Figure 4**a, where the number density can be controlled in the range of 6.2×10^6 / in^2 to 3.3×10^7 / in^2 (corresponding to surface coverage ranging of 11.45% to 16.50%). The strategy for adjusting surface density is described in Figure 4b. During phase I, the condensation of monomer droplets involves the coalescence of adjacent droplets to form larger droplets. Thus, by extending the condensation tie of phase I, we could grow larger BzMA monomer droplets with greater distance between them. To adjust the distance while keeping the PDA size unchanged, we polymerized the larger monomer droplets at a lower T_{fil} (220 °C). On the other hand, for shorter condensation times in phase I, densely packed smaller BzMA monomer droplets could be grown. Polymerizing these droplets at a higher T_{fil} (340 °C) yielded high coverage of PDAs (while keeping the average PDA sizes comparable to the previous case). This demonstrates our ability to fully control the geometric properties of PDAs, including size, radius of curvature, and surface particle density.

2.3 Mechanisms of tailoring PDA morphologies

Phase I of the CDP process comprises the condensation of monomer droplets, which has been extensively studied in previous work.[8c] However, there is still a lack of understanding regarding the important reaction mechanisms and kinetics in phases II and III, as well as

characterization with single-particle precision. To address those knowledge gaps, we formulate a theoretical framework below to explain how PDA morphologies can be precisely tailored during phases II and III.

2.3.1 Phase II: Radical polulations at different T_{fil} influence the polymerization kinetics

Our firt insight draws upon the existing experimental and computational results in radical chemistry, which attributed the larger PDA size and radius of curvature at higher T_{fil} to the different radical populations attainable at different T_{fil}.

Upon heating, the initiator TBPO undergoes a two-step thermal degradation (Figure 1c). Radical *t*-BuO• arises from the homolytic cleavage of the O-O bond in TBPO, which has a dissociation energy of 164 kJ mol^{-1}.[13] We use that dissociation energy as an estimate for the activation energy, which is a common treatment in the literature in the context of radical formation.[9a] Subsequently, *t*-BuO• undergoes *β*-scission to generate acetone and CH_3• (Figure S5, Supporting Information). Recent quantum chemical calculations have revealed an activation energy of 56 kJ mol^{-1} and a reaction enthalpy of 16 kJ mol^{-1} for this *β*-scission.[14] Based on the activation energies, we concluded that (***i***) the homolytic cleavage is the rate-limiting step, and the *β*-scission is rapid and often at equilibrium, and (***ii***) the equilibrium favors the products, i.e., acetone and CH_3• at higher reaction temperatures, i.e., T_{fil}, due to the overall endothermic process. This is also consistent with reported experimental results showing that the concentration of *t*-BuO• decreases while that of CH_3• increases as the T_{fil} exceeds 270 °C in iCVD.[9]

We attributed the larger PDA size to a faster rate of polymerization (R_p) at higher T_{fil}, due to the combined effects of radical reactivity and diffusivity in the polymerizing droplets. It is well established that CH_3• is more reactive than *t*-BuO•, as CH_3• exhibits high reactivity in both hydrogen abstraction and additional reactions.[15] Considering the molar volume of the two radicals, their diffusivities in the monomer droplets also differ significantly. The self-diffusion coefficient (D_0) of CH_3• and *t*-BuO• in BzMA monomer is calculated to be 3.06 × 10^{-9} and 1.29 × 10^{-9} cm^2 s^{-1}, respectively, at 10 °C using Stokes-Einstein equation. Based on the means-squared displacement (MSD = 6 ×D × t), the diffusion lengths of CH_3• and *t*-BuO• are estimated to be 43 nm and 28 nm, respectively, assuming an initiation and propagation time of $t \approx 1$ μs.[16] This suggests that CH_3• can access nearly 2 times the volume of a polymerizing drop before it reacts compared to that of *t*-BuO•. While as polymerization

progresses and the weight fraction of polymer increases, diffusivity gradually decreases, our theoretical calculation shows that CH_3• consistently retains the 2-fold higher diffusion coefficient than *t*-BuO• throughout the experimentally observed monomer conversion range (Figure S6, Supporting Information). Consequently, the greater reactivity and higher diffusivity of CH_3• is conducive to faster polymerization within each droplet at higher T_{fil}, resulting in larger PDA sizes.

To gain more insight into the effect of reactive radical species on the polymerization mechanism of PDAs during CDP, we conducted MALDI-TOF measurements (Figure S7, Supporting Information), and corresponding end-groups were investigated (Table S2, Supporting Information). Indeed, a higher overall occurrence of CH_3– end groups was observed at higher T_{fil}, indicating that CH_3• is the dominating species radical species. Interestingly, the variety of end groups in pBzMA increases with T_{fil}, suggesting more active chain transfer, which could be attributed to the higher molecular weight and entanglement of the concentrated pBzMA solution that hinders radical encounters. In addition, we quantified the monomer consumption as a function of T_{fil}, showing greater consumption at higher T_{fil} (Figure S8, Supporting Information), to corroborate the faster rate of polymerization (R_p) with increasing T_{fil}, which is consistent with the higher reactivity and diffusivity of CH_3• in the polymerizing droplets.

2.3.2 Phase III: Polymer solution evaporation dynamics affects PDA morphologies

Experimental studies on the drying of sessile droplets of polymer solutions have revealed that contact line pinning and depinning determine the final morphology of the dried polymer.[17] Importantly, in a solid-liquid-vapor system, the contact line friction was found to increase linearly with the viscosity of the liquid.[18] As such, we believe that the final morphology of the polymer domes is determined by the evolution of viscosity of the solution droplets throughout the polymerization and the occurrence of contact line pinning during the contraction (by evaporation).[19] Below, we detail how PDAs with different radii of curvature are caused by variations in the viscosity of the polymerizing droplets, which is, in turn, influenced by several factors during monomer evaporation, including polymer concentration and molecular weight. In addition, the interfacial energy at the vapor-liquid-solid interface could also affect the radii of curvature, which is discussed toward the end of this section.

We first discuss the effect of pBzMA concentration on viscosity. During phase III, monomer evaporation shrinks droplets and increases the polymer concentration.[17] It has been shown that pinning occurs in the average polymer concentration range of 20-40 wt%.[20] Therefore, the concentration of pBzMA in a droplet at the onset of phase III is particularly important, with a high concentration leading to early pinning and, thus, large radii of curvature and diameters for the resulting PDA.[20] That concentration could be directly determined by the monomer conversion (Figure S8, Supporting Information). Accordingly, one can imagine that the droplet of pBzMA solution generated at a higher T_{fil} could contact-line pin earlier. Conversely, the solution at lower T_{fil} results in PDAs with smaller radii of curvature due to the longer depinning period during phase III, which is consistent with our experimental observation (Figure 3i).

Viscosity has also been reported to be a function of the molecular weight of the polymer.[21] The molecular weight of PDAs created at different T_{fil} was characterized by GPC, and the PDAs exhibited weight-average molecular weight (M_w) of 28.6, 41.1, and 60.6 kg mol^{-1} at T_{fil} of 220, 280, and 340 °C, respectively (Figure S9 and Table S3, Supporting Information for details on the M_w, dispersity, etc.). Higher M_w is associated with a larger radius of gyration R_G (based on $R_G \sim M_w^{3/5}$), which reduces the overlap concentration c^*, i.e., the concentration at which polymer coils overlap (and thus drive up the viscosity), based on $c^* = 3Nb^3 / 4\rho\pi R_G^3$, where N is the number of repeat units, b = 1.8 nm is the Kuhn length of the monomer, ρ = 1.04 kg m^{-3} is the density of pBzMA (Table S3, Supporting Information).[21a] As a result, the viscosity of the droplets at the onset of phase III increases with M_w based on $\eta \sim c^{3.75} M_W^3$ (where c is solution concentration). Therefore, we argue that the contact line of the droplet of pBzMA solution at higher T_{fil} is more likely to be pinned during phase III as the solution becomes much more viscous than that of lower T_{fil} conditions. We attributed the distribution of the molecular weight of pBzMA PDAs to two factors during phase II: (i) the continuous supply of a large quantity of the initiator, (ii) the decrease in mobility of polymer chains, resembling bulk polymerization with a high degree of heterogeneity.

In addition to droplet viscosity, the interfacial energy at the vapor-liquid-solid interface plays a major role in determining the radii of curvature, where high molecular weight polymer solutions could form disk-like puddles due to increased contact line friction from strong adhesion of longer polymer chains to the substrate. To explore the interfacial energy of the droplets of polymer solutions, we obtained static contact angles of solutions of pBzMA

dissolved in its monomer at varying concentrations (Figure S10a, Supporting Information). The static contact angle of pure BzMA monomer was 88.93°, but it slightly increased with polymer concentration, as the contact angle of 20 wt% pBzMA solution was 98.37°. We also obtained the surface tension (interfacial free energy between liquid and gas, γ_{lg}) of these solutions through pendant droplet measurements (Figure S10b, Supporting Information), showing that the value of γ_{lg} remained almost constant with different polymer concentrations. Based on Young's Equation $\gamma_{lg} \cos\theta = \gamma_{sg} - \gamma_{sl}$, the energy differences between solid/gas interfacial energy (γ_{sg}) and solid/liquid interfacial energy (γ_{sl}) were determined. Given that the value of γ_{sg} does not change, this implies that γ_{sl} increases with polymer concentration. This further demonstrates that the interaction between the droplet of pBzMA solution and the substrate increases with polymer concentration.

Hence, we propose the mechanism of the formation of PDAs with different radii of curvature, as shown in Figure 4c. The enhanced adhesive effect hampers the polymer solution from receding, and thereby, contact line pinning occurs early during the evaporation process for PDAs under high T_{fil} conditions, resulting in the formation of domes with large radii of curvature.

2.4. Nanolens applications

This tunable radius of curvature offers various advantages in nano-lens optics, as it directly impacts the optical properties of the lens, such as focal length and aberrations. PDAs can be applied to plano-spherical convex lenses, where one side is flat (plano), and the other side is curved (convex) at the nanoscale. The curvature of the convex surface determines the lens's ability to converge or diverge light, and the precise control of the radius of curvature ensures the lens achieves the desired optical performance, such as focusing or magnification, without the need for bulky and expensive optical components.

Spectroscopic ellipsometry revealed that pBzMA exhibits refractive index (n) of 1.568 at 632.8 nm (Figure S11, Supporting Information), which is consistent with the literature.[22] Notably, this is similar to that of glass and immersion oil, enhancing the effectiveness of the lens by eliminating light beam deflection. Combined with this optical performance, the nearly perfect plano-spherical convex structure of PDAs makes CDP an ideal method for the high-throughput fabrication of well-defined nanoscale lenses. Recent demonstrations have shown that employing micro-nano scale lenses enables near-field focusing and magnification,

allowing the resolution of features beyond the diffraction limit.[7, 23] While a plethora of fabrication methods have been explored for micro/nano-lenses, including imprinting lithography,[5a, 24] inkjet printing,[6a] film dewetting,[25] optofluidics,[26] the high-throughput synthesis of micro-nano scale lenses with controlled morphologies remains a bottleneck.

Figure 5a illustrates the experimental configuration and mechanism used to demonstrate PDA lens applications using optical microscopy. We determined the theoretical focal length for each PDA lens manufactured at different T_{fil} (Figure S12, Supporting Information). Based on the focal length and the thickness of the coverslip, we oriented the convex side of the PDA lenses towards the specimen to ensure a sufficient magnification effect despite spherical aberration effect. It should be noted that coverslip #1 has an approximate thickness of 150 µm, which is approximately 4 to 7 times greater than the focal length of PDA lenses. If the object is positioned at a distance greater than twice the focal length, the resulting image will be inverted and appear reduced in size (Figure S13, Supporting Information). Figures 5b-d depict digital microphotography of the sub-micron scale line patterns on a resolution target, captured through a bare glass coverslip (Figure 5b) and through coverslips with pre-fabricated PDA lenses (Figure 5c). Based on the image with a bare glass coverslip, the resolution limit for digital microscopy appears to be approximately 2 µm, which is insufficient to resolve the line patterns with a line spacing of 600 lp/mm (approximately 1.67 µm, Figure 5b). In contrast, both the captured image (Figure 5c) and the line profiles (Figure 5d) indicate that the line patterns are distinctly resolved through the coverslip with PDA lenses. Additionally, we employed a high-resolution optical microscope to capture transmittance mode images of the same sample setup (Figure 5e, f). The optical images were obtained using a 40× objective lens with a reported numerical aperture (NA) of 0.6, corresponding to the Abbe diffraction limit of 417 nm ($r = 0.5\lambda/NA$). Although the optical micrograph does not resolve the line patterns with the line spacing of 1400 lp/mm (approximately 714 nm, Figure 5e), the PDA lenses enabled successful resolution in the high-resolution optical micrograph (Figure 5f). Notably, line profiles (blue and red lines, Figure 5g) demonstrate that PDA lenses significantly enhance the resolution through the magnification effect.

It is important to note that images captured with the PDA lens (Figure 5c, e) exhibit reduced resolution in areas outside the positions of the PDA lenses. This is due to the fact that images observed through the PDA lens and those in the surrounding area without the lens exist on different focal planes. While the PDA lens allows for more precise observation of smaller

details, as indicated in Figure 5a, the focus needs to be adjusted slightly closer to the objective lens. Nevertheless, the coverslip with PDA lens not only enhances optical resolution but also does not permit observation of the areas outside the PDA lenses by simply rotating the focusing knob. Furthermore, the mechanical robustness of the PDA lenses allows for multiple uses. Thus, PDA lenses can provide a feasible method for high-resolution optical imaging applications as follows.

To extend the application of PDA lenses to biological specimens, we examined mouse neutrophils stained with DAPI for nucleus DNA (blue) and anti-CD11n (APC conjugated) for the surface marker (red), which exhibited consistent sizes of 38.6 ± 10.7 μm^2 under a confocal microscope. When observing through the PDA microlenses, we captured an average neutrophil size (based on the DAPI-stained nuclei) of 54.3 ± 10.7 μm^2. This indicates that the PDA lens magnifies the underlying object by approximately 40%. It should be noted that PDA lenses are compatible with biological specimens for magnification in an aqueous environment using water or aqueous buffer solutions. Due to their mechanical robustness and durability, we were able to reuse PDA-fabricated glass coverslips multiple times.

Another significant advantage of PDA lenses produced by CDP is the ability to manipulate the radius of curvature, enabling control over magnification factors. To demonstrate this, we explored mouse peripheral red blood cells under a digital microscope (Figure S14, Supporting Information). The series of images show that PDA lenses prepared at different T_{fil} values exhibit distinct magnification factors ($M = l' / l$, based on the diameter of the cells), i.e., ~1.30 (5.63/4.33 μm), 1.45 (6.06/4.18 μm), and 2.08 (8.45/4.06 μm) for T_{fil} of 220, 280, and 340 °C, respectively. The versatility of CDP, which enables the production of PDAs with diverse morphologies and surface densities, points to a wide range of objects for magnification, irrespective of their size, population, and materials, etc.

To further demonstrate the ability of the PDA lenses to enhance focusing, we analyzed 500 nm fluorescent beads under the green excitation (488 nm) and emission (510 nm) using confocal microscopy (Figure S15, Supporting Information). The fluorescent images were obtained through a 40× objective lens with a numerical aperture (NA) of 1.2. Strikingly, the fluorescence images of green emitting beads without PDA lenses show a broader diameter with a full-width half maximum (FWHM) of 543 nm, whereas those of beads with PDA lenses appear smaller with an FWHM of 462 nm. This demonstrates that PDA lenses

simultaneously magnify underlying objects and focus visible lights to increase the resolution of microscopy.

3. Conclusion

In conclusion, the CDP process represents a promising synthesis platform for the high-throughput fabrication of micro-nano scale PDAs. Unlike previous methodologies, we have demonstrated precise control over the geometric properties of PDAs, including size, surface density, and radius of curvature, by manipulating the rheological properties of the droplet of the polymer solution by adjusting a key synthesis parameter, T_{fil}. This innovative approach allows for unprecedented control over the morphology of PDAs, which is a significant advancement over earlier works that lacked such precision. Our exploration of the rheological properties and polymer solution dynamics in the morphological evolutions of PDAs under dynamic conditions is framed within a theortical context that integrates coupled polymerization and non-equilibrium phase transitions. This theoretical framework not only clarifies the evaporation mechanism involoved but also sheds light on advanced applications such as inkjet printing, coating, and evaporative cooling technologies.[17a, 21] The resulting PDAs exhibit nearly perfect plano-spherical convex structures, coupled with the favorable refractive index of pBzMA, making them exceptionally effective lenses for magnification and focusing of optical signals. This capability represents a notable improvement in lens design, as our experimental findings reveal a significant enhancement in resolution achieved with PDA lenses in both digital and high-resolution optical microscopy. Moreover, the ability to manipulate the radius of curvature of PDAs provides precise control over magnification factors, further expanding the versatility and applicability of this technology across various fields, such as biological imaging, nanophotonics, and potentially biomaterials and drug delivery in the future. The rapid and scalable synthesis process of CDP, combined with the tunable optical properties of PDAs, this approach holds great potential for advancing the precision manufacturing of soft nanomaterials in optical imaging/photonics, sensing, and healthcare.

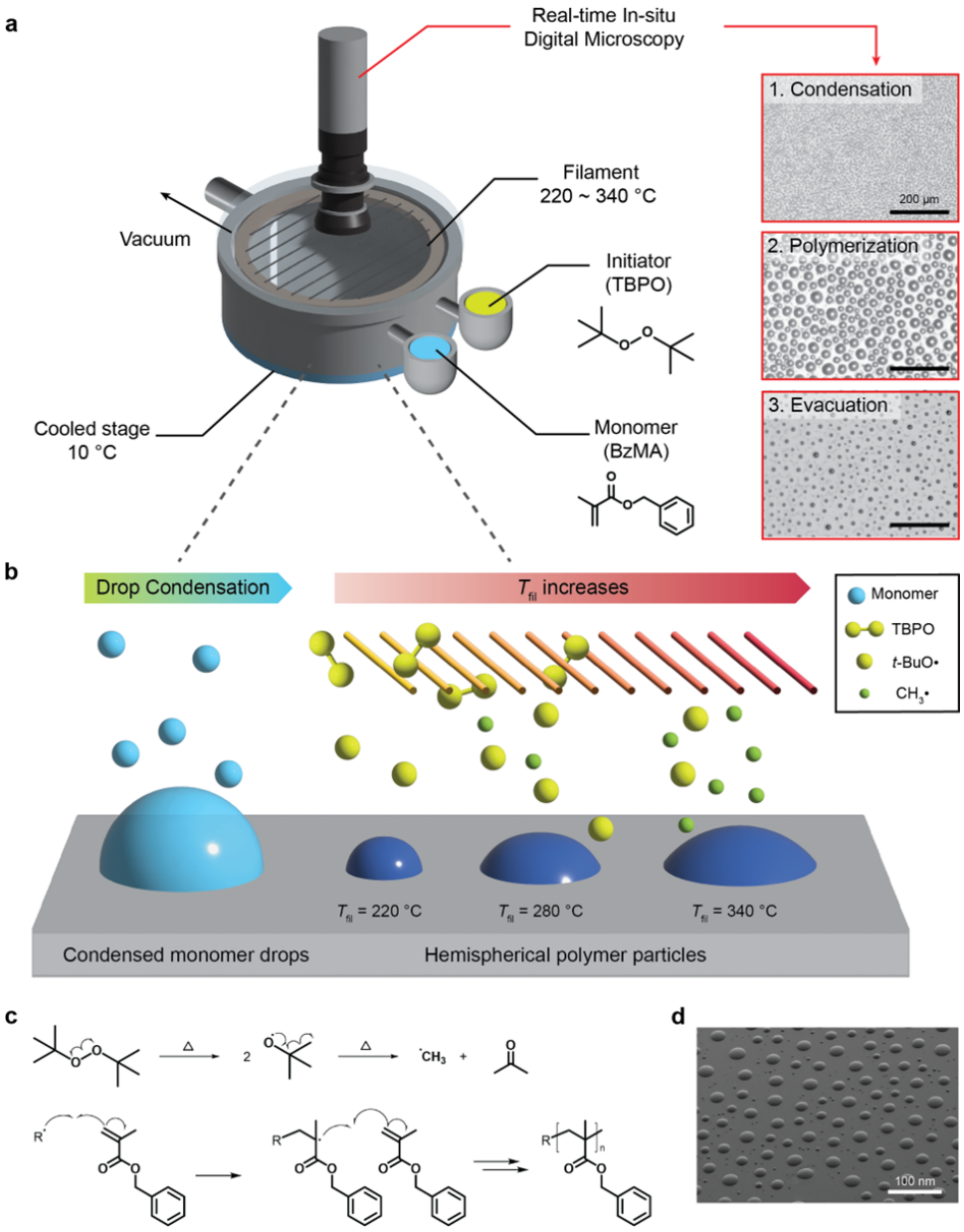

Figure 1. Schematic of CDP process a. CDP reactor consists of monomer, initiator inlets, vacuum, filament arrays, and cooled stage equipped with chiller. In-situ digital microscopy is installed for real-time monitoring (red images) during the CDP process. **b.** illustration of CDP process: monomer droplet condensation followed by polymerization and evacuation, showing the effect of T_{fil} on the surface morphologies. **c**. Reaction schemes of (top) decomposition of TBPO initiator and (bottom) free radical polymerization of BzMA monomer. **d.** Representative SEM image of PDAs.

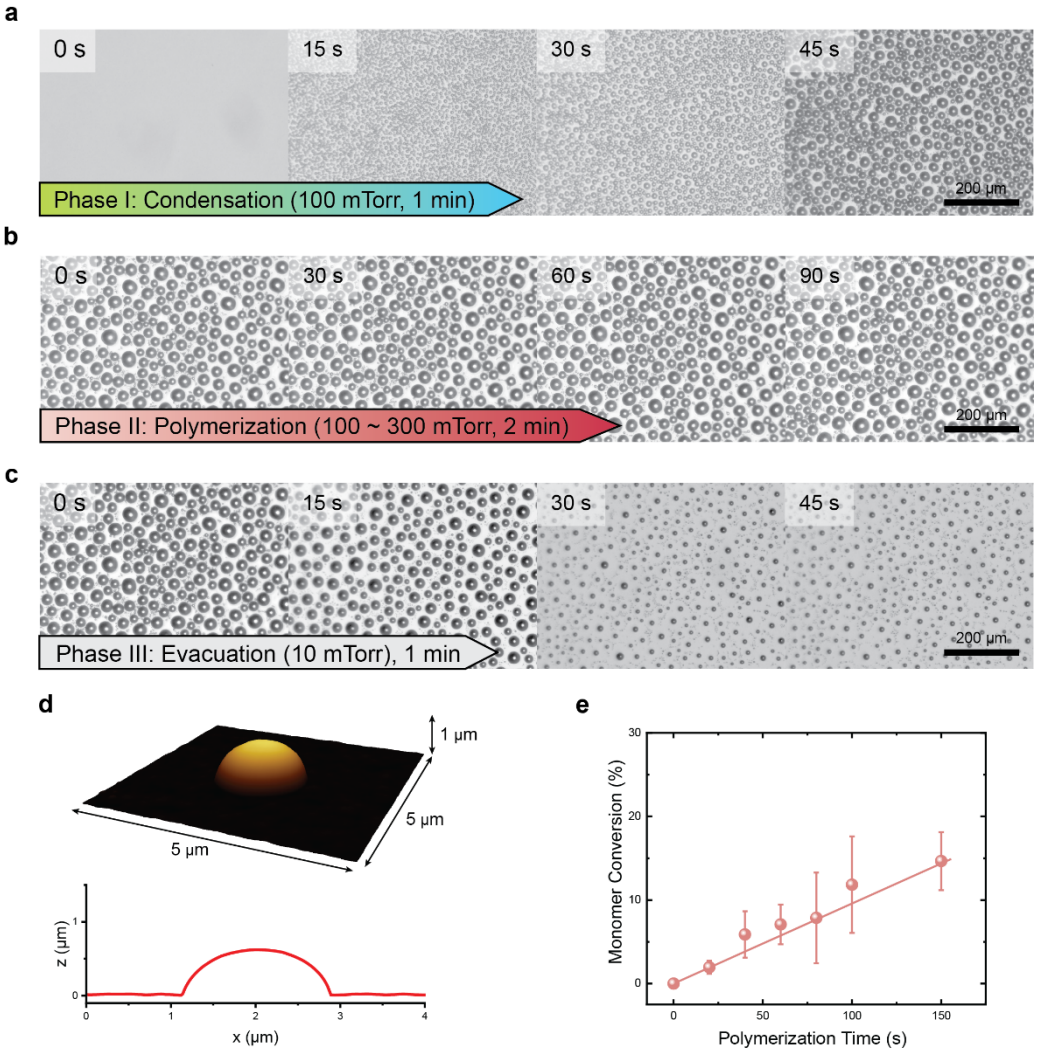

Figure 2. In-situ observations of CDP process. a-c. Digital microscopy images during (**a**) Phase I (monomer condensation), (**b**) Phase II (polymerization), and (**c**) Phase III (evacuation) processes. **d.** 3D AFM topography image of a single polymer dome (top) and corresponding plot of line profile (bottom). **e.** BzMA monomer conversion as a function of polymerization time (Phase II, at 300 mTorr, T_{fil} = 280 °C).

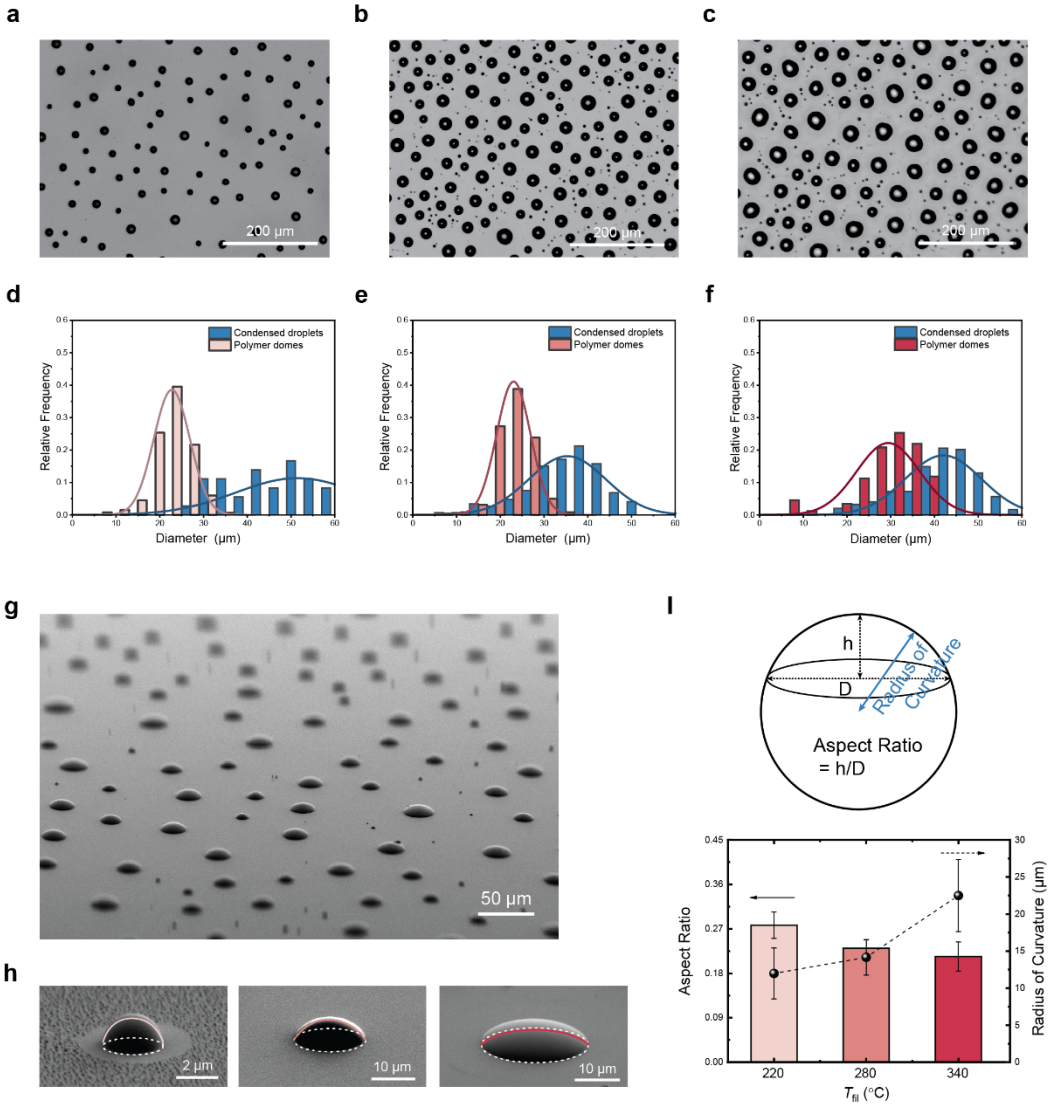

Figure 3. T_{fil} effect on the size of PDAs. a-c. Digital microscopy images of PDAs generated at T_{fil} of (**a**) 220, (**b**) 280, and (**c**) 340 °C. **d-f.** Histogram of the diameter of condensed monomer droplets (blue) and resulting PDAs (red) of corresponding PDAs generated at T_{fil} of (**d**) 220, (**e**) 280, and (**f**) 340 °C. **g.** Angled SEM image of PDAs. **h.** Representative SEM images of PDAs generated at T_{fil} of 220, 280, 340 °C from left to right, respectively. **i**. Plot of (left) the aspect ratio of height to diameter and (right) the radii of curvature as a function of T_{fil}.

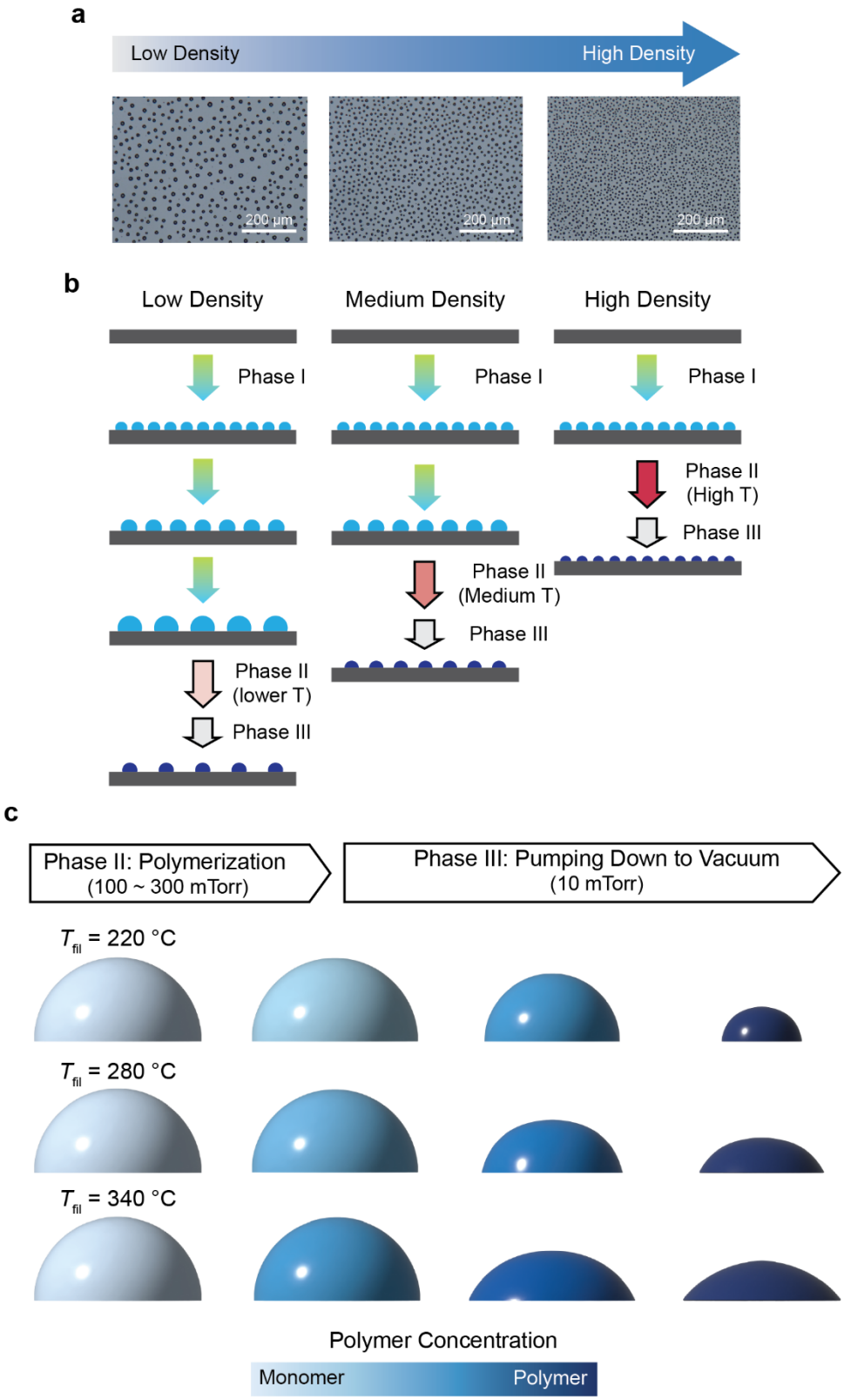

Figure 4. T_{fil} effect on the surface density of PDAs. a. Digital microscopy images of PDAS with different surface densities. **b**. Schematic of experimental procedures to obtain different surface density PDAs on the surface. **c.** The mechanism of the formation of different morphologies of PDAs based on polymer concentrations.

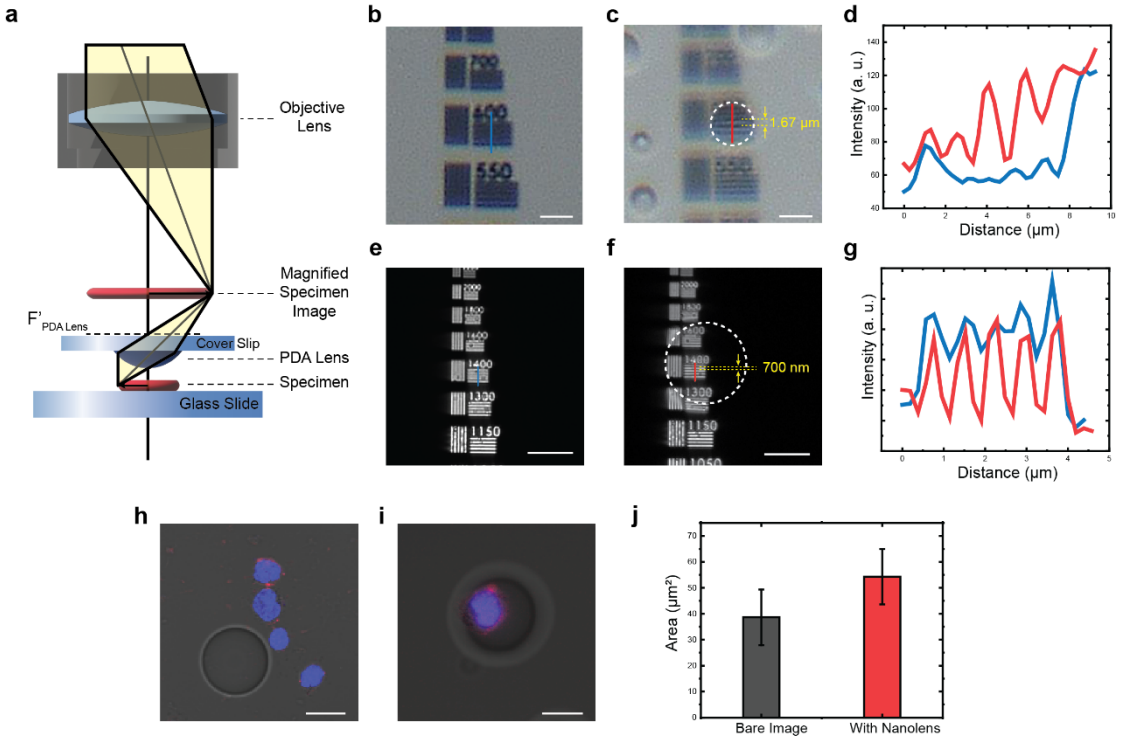

Figure 5. Application of the PDA plano-spherical convex lenses. a. Principle of the imaging process through the PDA lens. **b, c.** Digital microphotography of resolution target in reflection mode (**b**) without and (**c**) with PDA lens. **d.** Corresponding intensity profiles of blue and red lines indicated in Figures 5b and c, respectively. **e, f.** Optical microphotography of resolution target in transmittance mode (**e**) without and (**f**) with PDA lens. **g.** Corresponding intensity profiles of blue and red lines indicated in Figures 5e and f, respectively. **h, i.** Fluorescence images of the mouse neutrophils isolated from bone marrow (**h**) without and (**i**) with PDA lens, respectively; nucleus DNA was fluorescently labeled using 4',6-diamidino-2-phenylindole (DAPI, blue); surface antigen CD11b was labeled using corresponding antibody conjugated with allophycocyanin (APC, red). The scale bars represent 10 μm. **j**. Corresponding neutrophil size without (black) and with PDA lens (red). n = 86 for each group.

4. Experimental Section/Methods

Preparation of substrates: Si wafers were cleaned in 2% micro-90 solution, DI water, acetone, and 2-propanol, each in turn for 10 min using ultrasonication. After cleaning, the wafers were dried in N_2 flow. To fabricate poly(1H,1H,2H,2H-perfluorodecyl acrylate) (pPFDA) coatings, a cleaned Si wafer was placed inside an initiated chemical vapor deposition (iCVD) chamber. The coating thickness was monitored using a laser interferometer during the deposition, and the deposition was stopped when 100-nm-thick pPFDA film was deposited via iCVD, using conditions reported in the literature.[8a]

Condensed droplet polymerization (CDP): The pPFDA-coated Si substrates were placed on top of a thermoelectric cooling device (TEC, TE technology) that had been placed on the temperature-controlled chamber stage inside a vacuum chamber. A thermocouple was attached to the TEC to monitor the substrate temperature. The chamber was placed under vacuum and evacuated to approximately 3 mTorr. We kept the chamber stage cooled to 20-25 ℃ using a recirculating chiller (Accel 500 LT, Thermo Scientific). Additionally, we activated the TEC to cool below the chamber stage temperature using a DC power source (1715A, B&K Precision), maintained at 10 ℃ during the CDP process. The filament array (55% Cu/45% Ni alloy, Goodfellow) positioned a few inches above the substrate was heated to initiate the polymerization reaction. We varied the filament temperature from 220 to 340 ℃ by increasing the DC bias voltage. The temperature of the filament was monitored using a thermocouple. CDP was initiated only after the chamber was evacuated to a base pressure below 5 mTorr, upon which benzyl methacrylate (BzMA, Sigma-Aldrich, 96%) monomer vapors were introduced into the chamber. To vaporize the liquid BzMA monomer, we heated the monomer jar containing the liquid monomer to 85 ℃ using heated tape. During this stage, the chamber pressure was kept constant at 50 mTorr using a throttle valve (235B, MKS Instruments), and the vaporized monomers were condensed on the surface of the substrate. Throughout CDP, the time evolution of the size and morphology of the condensed droplets were monitored using an in-situ digital microscope (CHX 970F, Keyence). Once the monomer droplets reached the desired size (approximately 25-30 μm in diameter), we ceased the monomer flow into the chamber to halt the condensation.

We instigated the polymerization of the condensed monomer droplets by introducing *tert*-butyl peroxide (TBPO, Sigma-Aldrich, 98%) vapor into the chamber through a mass flow controller (MFC, 1152C, MKS Instruments). TBPO molecules were thermally decomposed upon passing through the heated filament array, forming *t*-BuO• and/or CH_3• to initiate

polymerization upon reaching the surface of the condensed droplets. During the polymerization, the chamber pressure was kept constant under 300 mTorr, after 120 s, CDP was stopped by evacuating the chamber to remove the residual initiator and monomer vapors.

Image analysis: Using the in-situ digital microscope images captured during each CDP run, the size and surface area of the condensed monomer droplets and resulting polymer particles were analyzed through ImageJ software.18 we only considered primary monomer droplets (with diameters greater than 10 μm) and the resulting polymer domes due to the resolution limit of the digital microscope.

Scanning electron microscopy (SEM): We utilized SEM (Gemini 500, Zeiss) to obtain detailed morphological information, such as diameter, height, and aspect ratio of the polymeric nano- and micro-domes. SEM was operated with an acceleration voltage of 1-2 kV, and the samples were sputter-coated with 3 nm of gold/palladium.

Contact angle: We used a contact angle goniometer (Model 500, ramé-hart) to collect monomer contact angles on the pPFDA-coated substrates. Monomer drops of 2 μL were dispensed onto the substrate through an automated dispensing system, and we measured the contact angle more than three times for each monomer.

Atomic force microscopy (AFM): AFMs (Cyper ES and MFP-3D, Oxford Instruments) were utilized to observe the topography of the polymer particles as well as characterize the mechanical properties of particles. We used Al-coated AFM probes (PPP-NCR, Nanosensors, F ≈ 26 N/m). Topography images were obtained through the conventional tapping mode.

Size exclusion chromatography: CDP was performed on a 4-inch pPFDA-coated Si wafer twice and the polymer particles were collected through ultrasonication for 5 min in 2-propanol. After 2-propanol was fully desiccated, the resulting polymer particles were dissolved in DMF with 0.05% LiBr as an eluent. We performed size exclusion chromatography (Ambient Temperature GPC: DMF, Waters^{TM}) measurements of the sample solutions. Poly(methyl methacrylate) standards were used to calibrate the molecular weights of the polymer domes produced via CDP.

MALDI-TOF: CDP was performed on a 4-inch pPFDA-coated Si wafer twice and the polymer particles were collected through ultrasonication for 5 min in 2-propanol. After 2-propanol was fully desiccated, the resulting polymer particles were dissolved in acetone with a concentration of approximately 2 mg/mL. Subsequently, dihydroxybenzoic acid and *trans*-3-indoleacrylic acid were used as MALDI matrices, and they were dissolved in acetone with a concentration of 15 mg/mL. 20% (v/v) of water was added to the final matrix solution to slow down drying and facilitate the crystal formation. The matrix and sample solutions were mixed by combining 2 μL of the sample and 10 μL of the matrix solution. The mixture was vortexed briefly, and thereafter, 0.5 μL was applied to the MALDI plate.[27]

Animal maintenance and cells: Healthy male BALB.C mice aged 4 to 6 weeks were procured form the Jackson Laboratory (NY). All animals were raised and cared for according to the animal experimental protocols approved by the Institutional Animal Care and Use Committee (IACUC) in conjunction with the Animal Use Guidelines established by the Cornell University Center of Animal Resources and Education (CARE).

Preparation of mouse red blood cell slides: Male BALB/C mice were subjected to anesthesia, and peripheral blood samples of 10 ~ 20 μL were collected via the retroorbital vein into heparin pre-treated tubes to prevent coagulation. Subsequently, blood smears were carefully applied onto slides pre-treated with L-lysine, facilitating subsequent optical microscopic analysis.

Isolation and staining of the mouse neutrophils: Due to the difficulty of getting a sufficient quantity of neutrophils from the peripheral blood of mice, we isolated mice neutrophils from bone marrow. Male BALB/C mice were euthanized and immersed in 70% ethanol for 10 min to ensure full sterilization. The femur and tibia, along with the attached muscle tissue, were meticulously separated, followed by sterilization of the collected bones using 70% ethanol and subsequent washing with pre-chilled buffer (0.5% BSA and 2 mM EDTA in PBS, pH 7.2). Bone marrow cells were harvested by thorough flushing of the bone cavity with the aforementioned buffer and subsequent centrifugation at 400 × g, 4 ℃ for 5 min. The resulting pellet was suspended in 10 ml of 0.2 % sterile NaCl solution to lyse the red blood cells, with osmotic pressure restored by mixing the solution with 10 ml of 1.6% sterile NaCl solution after 30 s. The cell suspension was filtered through a 70 μm sterile cell strainer (SIAL-CLS431751, Sigma-Aldrich-Corning) and centrifuged at 400 × g, 4 ℃ for 5 min. The result

pellet was suspended with 1 ml PBS for subsequent purification. In a 15 ml sterile tube, 5 ml Histopaque-1077 (1.077 g/ml), 1 ml bone marrow cell suspension, and 5 ml Histopaque-1119 (1.119 g/ml) were carefully layered from the bottom to the top without agitation. Neutrophils were collected following centrifugation at 100 × g, 4 ℃ for 30 min, and washed twice with RPMI-1640 medium (12633012, Thermo Fisher Scientific). To assess the purity of the isolated neutrophils, cells were stained with an antibody mixture comprising equal amounts of Anti-Mouse CD11b antibody (Allophycocyanin, APC, 101211, Biolegend) and Anti-Ly-6G antibody (Brilliant Violet reg 421, 127627, Biolegend) at a dose of 0.2 μg per 10^6 cells in 100 μl PBS on ice. The fraction of neutrophils was ~70%, as confirmed by flowcytometry.

The isolated neutrophils were stained with 1 μg/ml 4',6-diamidino-2-phenylindonle (DAPI) and Anti-mouse CD11n Antibody (APC, 101211, Biolegend) at a dose of 0.1 μg per 10^6 cells in 100 μl PBS on ice for 1 hr. Subsequently, cells were washed with PBS, fixed with 4% paraformaldehyde at room temperature, and applied onto L-lysine pre-treated slides for subsequent optical microscopy imaging and analysis.

Optical microscopy: Olympus BX41 optical microscope was used in both reflectance and transmittance mode, with a 40× objective lens with a numerical aperture (NA) of 0.65 and a 40× eyepiece. Confocal microscopy was performed using a Zeiss LSM710 confocal microscope for fluorescent sample imaging, using a 40× objective lens with a NA of 1.20 and a 10× eyepiece.

Supporting Information

Supporting Information is available from the Wiley Online Library or from the author.

Acknowledgements

This research was financially supported by the National Science Foundation Faculty Early Career Development Program (CMMI-2144171). This work made use of the facilities and instrumentation supported by NSF through the Cornell University Materials Research Science and Engineering Center DMR-1719875. The authors would like to express our sincere gratitude to Prof. Warren Zipfel for his invaluable support and discussion throughout this research. His expertise and insights greatly contributed to the success of this work. The authors also gratefully acknowledge technical and facility support provided by the Cornell Energy Systems Institute (CESI). Imaging data was acquired through the Cornell Institute of

Biotechnology's Imaging Facility, with NIH 1S10RR025502 funding for the shared Zeiss LSM 710 Confocal Microscope. S.S.L. was supported by the Natural Sciences and Engineering Research Council of Canada through CGS-D.

Received: ((will be filled in by the editorial staff))
Revised: ((will be filled in by the editorial staff))
Published online: ((will be filled in by the editorial staff))

References

[1] a)B. Bhushan, Y. C. Jung, *Progress in Materials Science* **2011**, 56, 1; b)W.-G. Bae, H. N. Kim, D. Kim, S.-H. Park, H. E. Jeong, K.-Y. Suh, *Advanced Materials* **2014**, 26, 675.

[2] P. Vukusic, J. R. Sambles, *Nature* **2003**, 424, 852.

[3] a)J. Yong, F. Chen, Q. Yang, G. Du, H. Bian, D. Zhang, J. Si, F. Yun, X. Hou, *ACS Applied Materials & Interfaces* **2013**, 5, 9382; b)E. P. Chan, A. J. Crosby, *Advanced Materials* **2006**, 18, 3238; c)S. Thiele, K. Arzenbacher, T. Gissibl, H. Giessen, A. M. Herkommer, *Science Advances* **2017**, 3, e1602655; d)M. Marini, A. Nardini, R. Martínez Vázquez, C. Conci, M. Bouzin, M. Collini, R. Osellame, G. Cerullo, B. S. Kariman, M. Farsari, E. Kabouraki, M. T. Raimondi, G. Chirico, *Advanced Functional Materials* **2023**, 33, 2213926.

[4] a)J. Qian, S. Kolagatla, A. Pacalovas, X. Zhang, L. Florea, A. L. Bradley, C. Delaney, *Advanced Functional Materials* **2023**, 33, 2211735; b)Y. Zhan, F. Hou, S. Feng, X. Wang, W. Sun, J. Ye, Y. Zhang, *Advanced Optical Materials* **2022**, 10, 2102548.

[5] a)D.-H. Ko, J. R. Tumbleston, K. J. Henderson, L. E. Euliss, J. M. DeSimone, R. Lopez, E. T. Samulski, *Soft Matter* **2011**, 7, 6404; b)F. Galeotti, F. Trespidi, G. Timò, M. Pasini, *ACS Applied Materials & Interfaces* **2014**, 6, 5827; c)A. Papadopoulos, E. Skoulas, A. Mimidis, G. Perrakis, G. Kenanakis, G. D. Tsibidis, E. Stratakis, *Advanced Materials* **2019**, 31, 1901123.

[6] a)S. Liu, X. Liao, L. T. de Haan, Y. You, H. Ye, G. Zhou, D. Yuan, *Soft Matter* **2021**, 17, 748; b)C. Li, Y. Yu, H. Li, J. Tian, W. Guo, Y. Shen, H. Cui, Y. Pan, Y. Song, H. C. Shum, *Nano Letters* **2022**, 22, 5236; c)X. Liu, J. Li, P. Zhang, W. Lu, G. Yang, H. Zhong, Y. Zhao, *Nano Research* **2022**, 15, 7681.

[7] J. Y. Lee, B. H. Hong, W. Y. Kim, S. K. Min, Y. Kim, M. V. Jouravlev, R. Bose, K. S. Kim, I.-C. Hwang, L. J. Kaufman, C. W. Wong, P. Kim, K. S. Kim, *Nature* **2009**, 460, 498.

[8] a)T. Franklin, D. L. Streever, R. Yang, *Chemistry of Materials* **2022**, 34, 5960; b)T. Franklin, R. Yang, *Chemistry of Materials* **2023**, 35, 4955; c)J. James, R. Yang, *Organic Materials* **2023**, 5, 148.

[9] a)G. Ozaydin-Ince, K. K. Gleason, *Journal of Vacuum Science & Technology A* **2009**, 27, 1135; b)P. Moni, H. S. Suh, M. Dolejsi, D. H. Kim, A. C. Mohr, P. F. Nealey, K. K. Gleason, *Langmuir* **2018**, 34, 4494.

[10] P. A. Lovell, F. J. Schork, *Biomacromolecules* **2020**, 21, 4396.

[11] C. Cheng, M. Gupta, *Industrial & Engineering Chemistry Research* **2018**, 57, 11675.

[12] J. Chen, Z. Zeng, J. Yang, Y. Chen, *Journal of Polymer Science Part A: Polymer Chemistry* **2008**, 46, 1329.

[13] J. Brandrup, E. H. Immergut, E. A. Grulke, A. Abe, D. R. Bloch, *Polymer handbook*, Vol. 89, Wiley New York, **1999**.

[14] R. Oyama, M. Abe, *The Journal of Organic Chemistry* **2020**, 85, 8627.

[15] D. H. Volman, R. K. Brinton, *The Journal of Chemical Physics* **1952**, 20, 1764.

[16] J. Kubečka, F. Uhlík, P. Košovan, *Soft Matter* **2016**, 12, 3760.

[17] a)I. G. Hwang, J. Y. Kim, B. M. Weon, *Applied Physics Letters* **2017**, 110; b)G. K. S. Raghuram, L. Bansal, S. Basu, A. Kumar, *Colloids and Surfaces A: Physicochemical and Engineering Aspects* **2021**, 612, 126002.

[18] M. Ramiasa, J. Ralston, R. Fetzer, R. Sedev, *The Journal of Physical Chemistry C* **2011**, 115, 24975.

[19] D. Brutin, *Droplet wetting and evaporation: from pure to complex fluids*, Academic Press, **2015**.

[20] J. Fukai, H. Ishizuka, Y. Sakai, M. Kaneda, M. Morita, A. Takahara, *International Journal of Heat and Mass Transfer* **2006**, 49, 3561.

[21] a)K. A. Baldwin, D. J. Fairhurst, *Colloids and Surfaces A: Physicochemical and Engineering Aspects* **2014**, 441, 867; b)D. Mamalis, V. Koutsos, K. Sefiane, A. Kagkoura, M. Kalloudis, M. E. R. Shanahan, *Langmuir* **2015**, 31, 5908.

[22] J. Park, K. Char, C. W. Park, *Industrial & Engineering Chemistry Research* **1999**, 38, 4675.

[23] Z. Wang, W. Guo, L. Li, B. Luk'yanchuk, A. Khan, Z. Liu, Z. Chen, M. Hong, *Nature Communications* **2011**, 2, 218.

[24] X. Zhu, Q. Xu, Y. Hu, H. Li, F. Wang, Z. Peng, H. Lan, *Optics & Laser Technology* **2019**, 115, 118.

[25] A. Verma, A. Sharma, *Advanced Materials* **2010**, 22, 5306.

[26] N.-T. Nguyen, *Biomicrofluidics* **2010**, 4.

[27] A. Nordborg, K. Irgum, *Journal of Applied Polymer Science* **2010**, 117, 2781.

Supporting Information

Polymer Microarray with Tailored Morphologies through Condensed Droplet Polymerization for High-Resolution Optical Imaging Applications

*Kwang-Won Park[1], Sophie S. Liu[1,2], Wenjing Tang[1], and Rong Yang[1,2]**

[1]Robert F. Smith School of Chemical & Biomolecular Engineering, Cornell University, Ithaca, NY 14853, United States

[2]Meinig School of Biomedical Engineering, Cornell University, Ithaca, NY 14853, United States

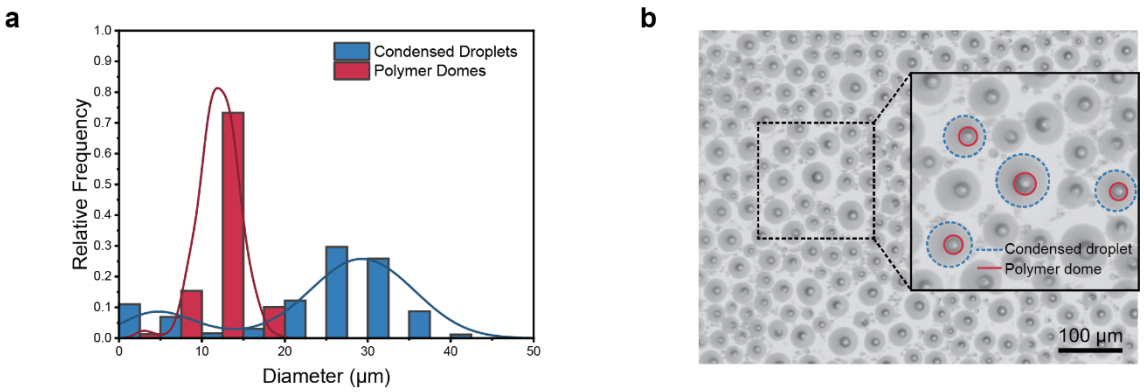

Figure S1. (a) Histogram of the diameter of condensed monomer droplets (blue) and resulting PDAs (red). (b) Superimposed image of the last stages of Phase II and Phase III to compare the sizes before and after polymerization.

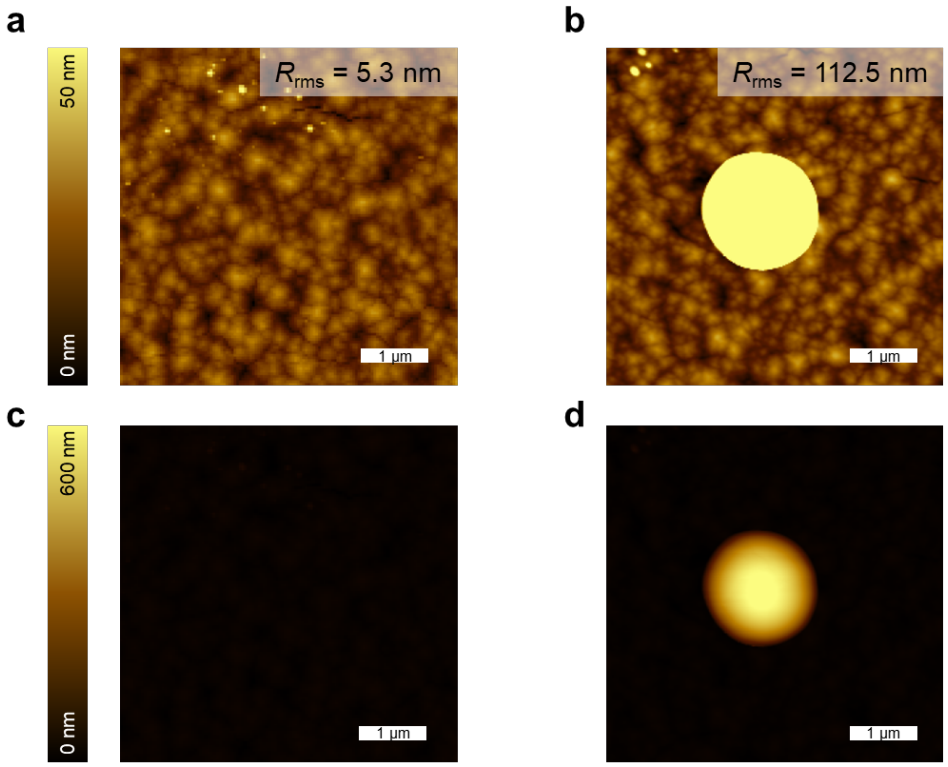

Figure S2. AFM topography images of (a, c) bare pPFDA surface and (b, d) pBzMA dome on pPFDA surface with color mapping (a, b) between 0 to 50 nm and (c, d) between 0 to 600 nm.

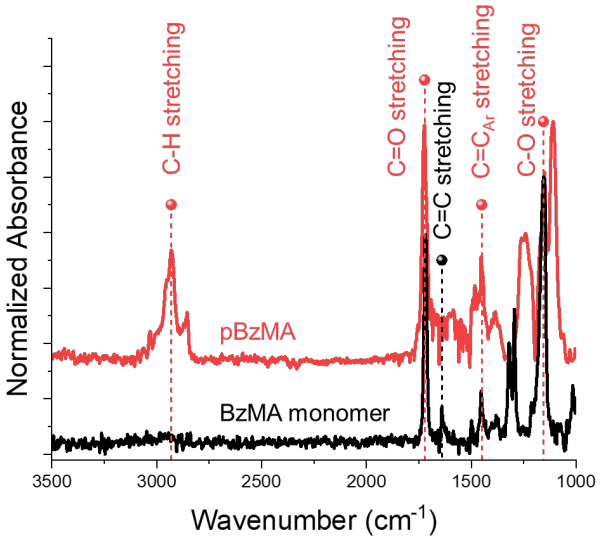

Figure S3. FT-IR spectra of BzMA monomer (black) and pBzMA (red).

Table S1. Experimental conditions of CDP process and diameter of monomer droplets and polymer domes.

Partial pressure (mTorr)		T_{sub} (°C)	T_{fil} (°C)	Polymerization Time (s)	Monomer droplet size (μm)	Polymer dome size (μm)
BzMA	TBPO					
50	100	10	220	120	35.7 ± 5.4	12.6 ± 1.6
		10	280		36.7 ± 6.5	14.3 ± 2.3
		10	340		34.7 ± 4.7	14.1 ± 2.5
50	200	10	220	120	33.6 ± 6.5	14.8 ±1.9
		10	280		37.0 ± 8.7	17.3 ± 3.6
		10	340		34.1 ± 8.8	19.8 ± 3.1
50	300	10	220	120	51.4 ± 12.1	21.1 ± 3.9
		10	280		35.3 ± 8.7	23.0 ± 3.8
		10	340		42.1 ± 8.8	31.2 ± 6.7

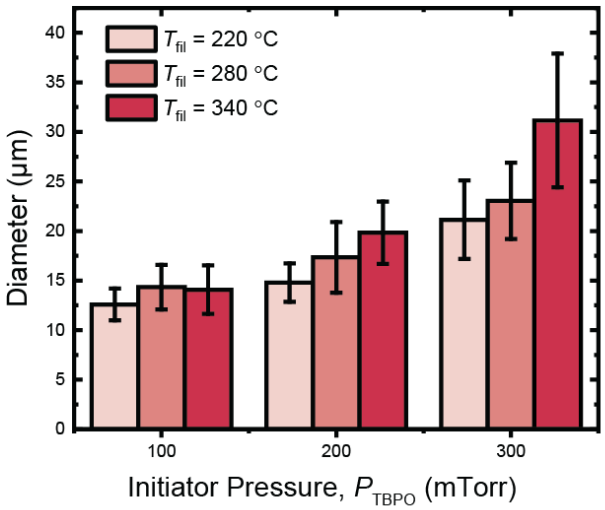

Figure S4. Diameter of PDAs prepared at different CDP reaction conditions (varying T_{fil} and P_{TBPO}).

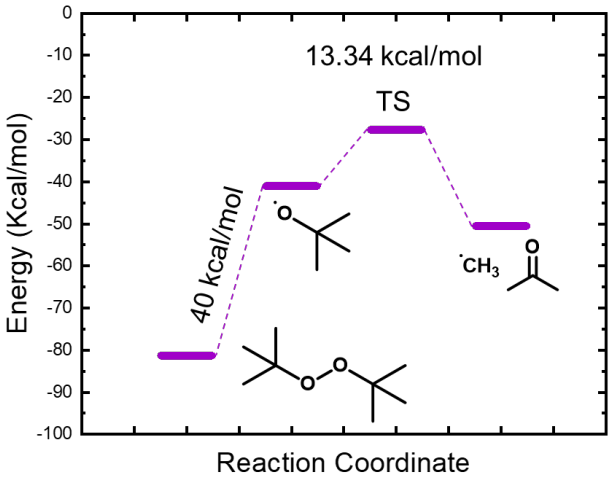

Figure S5. Energy diagram of homolytic cleavage of TBPO and subsequent *β*-scission reactions to generate acetone and CH_3•.

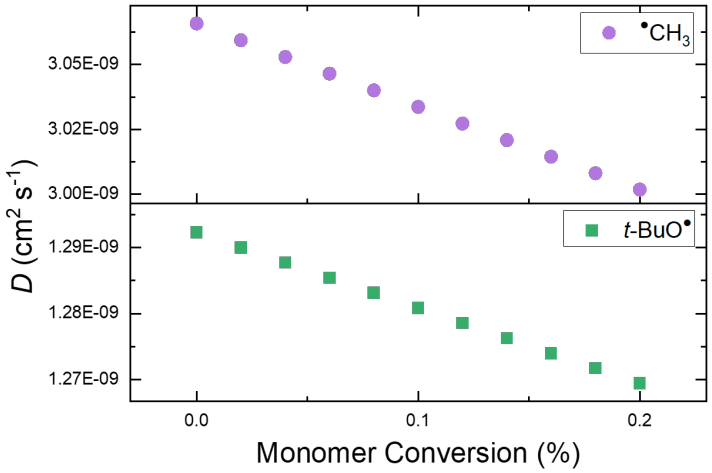

Figure S6. Diffusion coefficients of CH_3• (up, purple circle) and *t*-BuO• (bottom, green square).

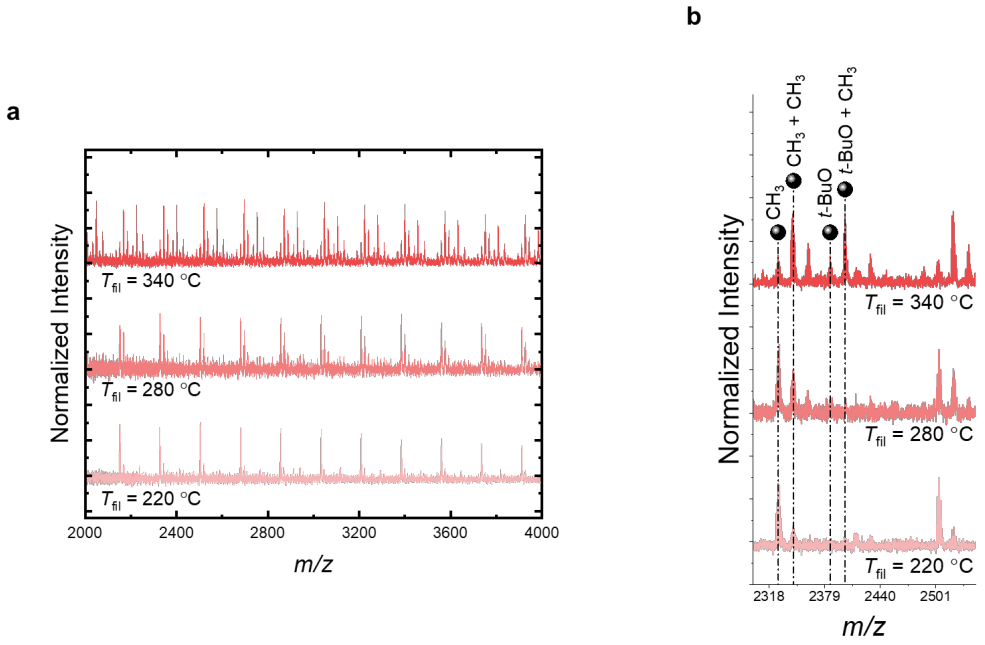

Figure S7. (a) MALDI-TOF spectra of pBzMA PDAs prepared at different T_{fil} (220, 280, and 340 °C). (b) Detailed MALDI-TOF spectra highlighting the peaks.

Table S2. Estimated percentages of end group occurrences from MALDI-TOF spectra at each T_{fil} conditions.

	T_{fil} (°C)	220	280	340
End Group Occurrence (%)	CH_3–	70.17	35.33	9.40
	CH_3– / CH_3–	18.58	21.68	24.18
	CH_3– / CH_3– + CH_3	-	11.10	13.75
	t-BuO–	-	7.05	9.05
	t-BuO– / CH_3–	-	7.04	24.47
	t-BuO– / CH_3– + CH_3	-	9.58	5.13
	t-BuO– / CH_3– + 2 CH_3	11.25	8.22	9.85
	t-BuO– / CH_3– + 3 CH_3	-	-	4.17
Total Occurrence of CH_3- (%)		88.75	92.95	90.95
Total Occurrence of *t*-BuO- (%)		11.25	31.89	52.67

MALDI-TOF revealed that the variety of end-groups increases for pBzMA as T_{fil} increases, pointing to a greater complexity in the termination mechanisms at higher T_{fil}, including combination, disproportionation, and chain transfer. At T_{fil} = 220 °C, 70.17% of the products had a single end-group (i.e., methyl), indicating that polymer chains were primarily terminated by disproportionation. The presence of multiple end-groups in 11.25% of the products, albeit in small amounts, suggests that branched polymer chains were created due to chain transfer to the polymer. This might be caused by the abrupt increase in the viscosity of pBzMA solution[1] during monomer evaporation, making combination less likely as radicals have difficulty encountering each other. At T_{fil} = 340 °C, however, approximately 50% of polymers have two end-groups, presumably generated by combination, while multiple combinations of products were assigned. Additionally, 33% of products had more than 2 end-groups, indicating that chain-transfer was more active than the process at lower T_{fil}. This might be due to the fact that the concentrated pBzMA solution is more entangled with higher molecular weight during Phase 3.[2] Also, BzMA introduces steric hinderance due to its considerably bulky substituent, i.e., benzyl ester moiety. Associated with the gel effect, the dynamics of polymer solution become extremely slow, making it even more difficult for radicals to encounter each other.[1]

However, we also observed that the occurrence of *t*-BuO end-groups increases with higher T_{fil} conditions, contradicting our assumption. This can be explained by two factors: (1) the probability of the homolysis of TBPO increases with higher T_{fil}, leading to an increase in the absolute number of *t*-BuO•; (2) the diffusion length of *t*-BuO• is longer and more effective at

higher T_{fil} because the higher effective temperature of the atmosphere not only enhances the MFP of radicals but also lower the collision frequency of radicals.

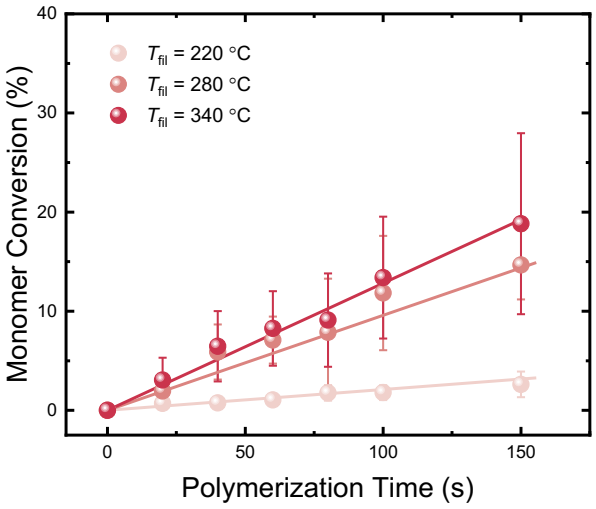

Figure S8. Monomer conversion (%) as a function of polymerization time (s) obtained at different T_{fil} (220, 280, 340 °C) under 300 mTorr.

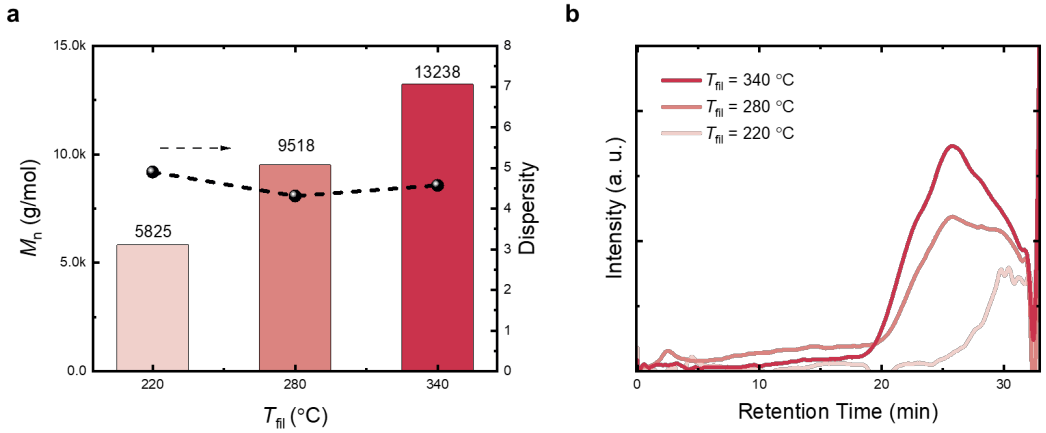

Figure S9. (a) Molecular weight (left) and corresponding dispersity of pBzMA PDAs generated at different T_{fil}. (b) GPC data as a function of retention time.

Table S3. Important parameters for the dynamic properties of pBzMA polymer solutions.

T_{fil} (°C)	M_w (kg/mol)	$Đ$	R_g (nm)	D_0 (μm^2 s^{-1})	c^*
220	28.6	4.90	4.59	1.77×10^{-1}	2.25
280	41.1	4.31	5.68	9.93×10^{-2}	1.71
340	60.6	4.57	7.13	5.36×10^{-2}	1.27

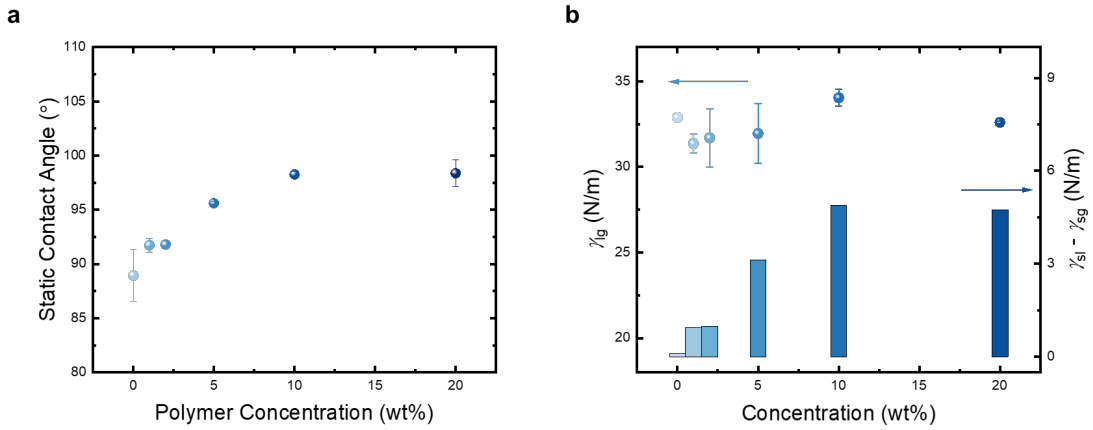

Figure S10. (a) Static contact angle of pBzMA solution in its monomer BzMA at different concentrations. (b) Corresponding interfacial energy between liquid and gas.

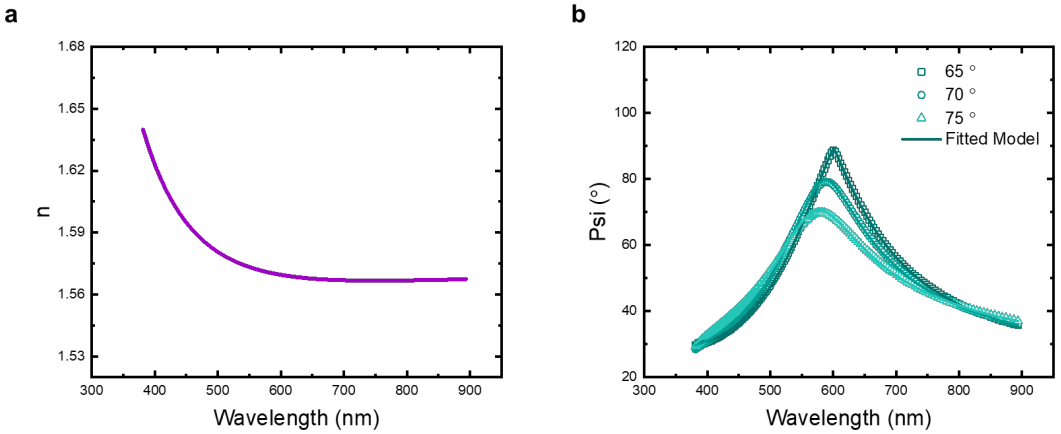

Figure S11. Spectroscopic ellipsometry data (a) refractive index (n) and (b) psi values as a function of wavelength.

T_{fil}	220	280	340
n		1.57	
NA		1.57	
Radius of Curvature (μm)	11.98	14.16	22.49
Focal Length (μm)	21.02	24.84	39.46

$$\frac{1}{f} = (n-1)\frac{1}{R}$$

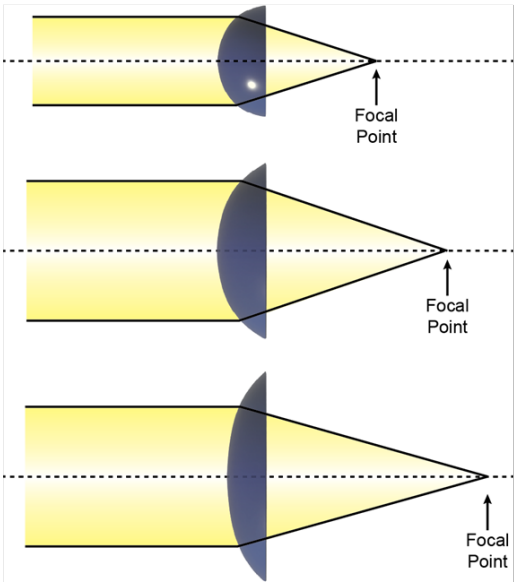

Figure S12. Theoretical focal length and numerical aperture (NA) values of PDAs estimated from the refractive index (n) and the radius of curvature (R).

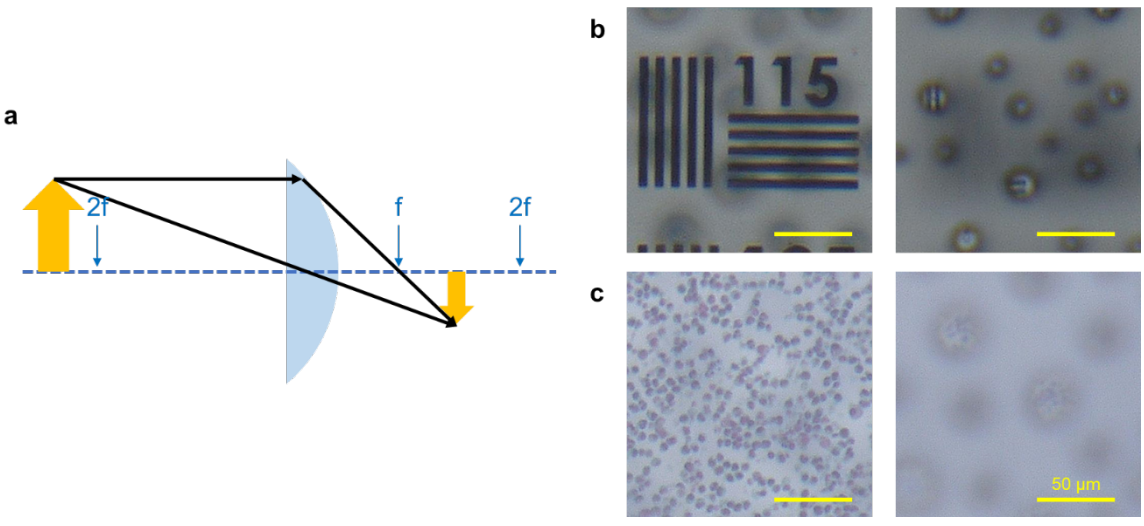

Figure S13. a. Schematic representation of the operation of a plano-convex spherical lens. b. Digital microphotography of resolution target using PDA lenses. The focal plane is (left) on the object and (right) on the real image. c. Digital microphotography of Nontypeable *Haemophilus influenzae* bacterias. The focal plane is (left) on the object and (right) on the real image.

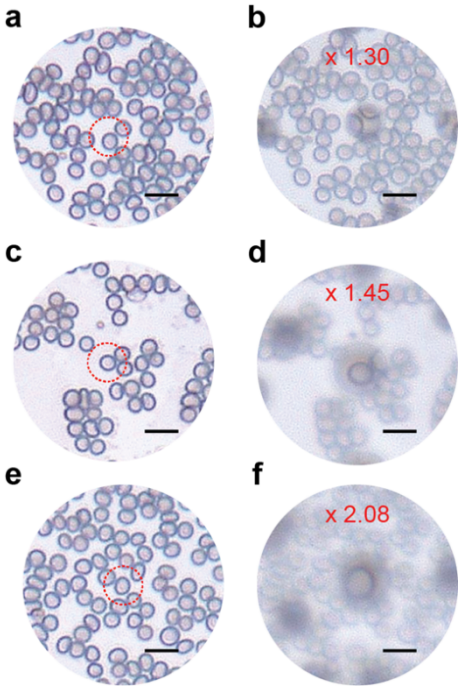

Figure S14. Mouse red blood cell images obtained via digital microscopy without (a, c, e) and with (b, d, f) PDA lenses created at different T_{fil} = (a, b) 220, (c, d) 280, and (e, f) 340 °C.

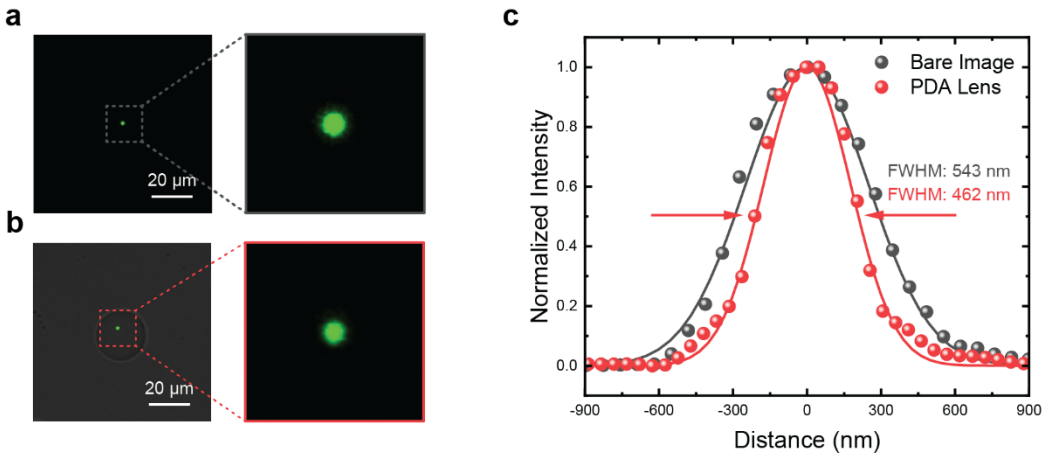

Figure S15. (a, b) Confocal microscope images of 500-nm fluorescent beads (a) without and (b) with PDA lens. (c). Corresponding point spread function by fitting the profile of the images in Figure S14a (Black, without PDA lenses) and b (Red, with PDA lenses) to a Gaussian function.

References

[1] Y. Suzuki, R. Mishima, E. Kato, A. Matsumoto, *Polymer Journal* **2023**, 55, 229

[2] M. Rubinstein, R. H. Colby, *Polymer physics*, Oxford university press, **2003**.